Final Technical Report

SISGR: Linking Ion Solvation and Lithium Battery Electrolyte Properties

Prof. Paul Trulove, U.S. Naval Academy

1. DOE Award # and Institution:
   - IAA No. DE-SC0001419
   - U. S. Naval Academy

2. Project title and name of the PI:
   - SISGR: Linking Ion Solvation and Lithium Battery Electrolyte Properties
   - PI: Paul C. Trulove

3. Date of the report and period covered by the report:
   - Date of Report: 30 Sept 2012
   - Period Covered: 15 Sep 2009 – 14 Sep 2012

4. A brief description of accomplishments:

Phase Behavior and Solvation of Lithium Triflate in Ethylene Carbonate, gamma-Butyrolactone, or Propylene Carbonate

Introduction

Due to the significant technological importance of lithium ion (Li-ion) batteries, extensive research effort is currently being directed towards understanding and improving their performance and properties (1). Fundamental studies in this research area have focused predominately on electrode materials (2-4) with relatively limited effort directed at Li-ion electrolytes, especially with respect to solvent–salt interactions (5).

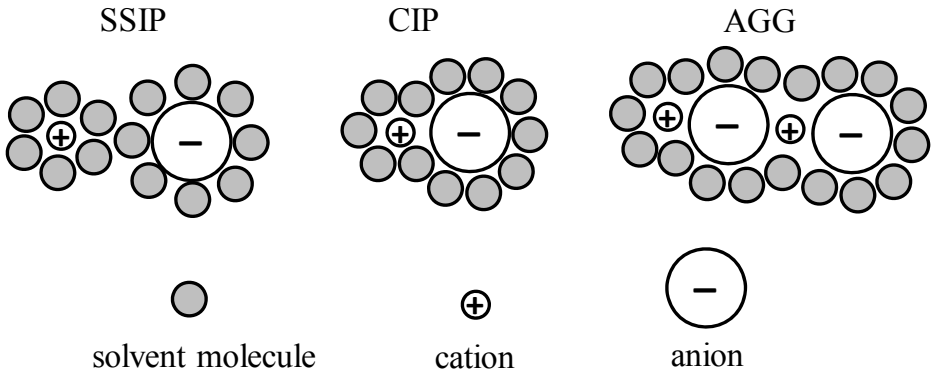

Figure 1. Cartoon depicting three general categories of solvent–salt interactions.

In an electrolyte, solvent–salt interactions are commonly characterized as falling into three general groups: solvent-separated ion pair (SSIP), contact ion pair (CIP), and aggregates (AGG) (7). Figure 1 is a cartoon depicting simplified versions of the three types of solvent–salt interactions. A SSIP consists of individually solvated ions and is

smaller than a CIP or AGG. In an electrolyte, the preferred solvation is a SSIP for two simple reasons: size and charge. The smaller volume displacement of solvent–salt in a SSIP means it will have a greater diffusion coefficient than CIPs or AGGs. Additionally, CIPs and AGGs have charge balancing ions in close proximity. The charge balance in CIPs and AGGs limits efficiency of charge transport as compared to SSIP.

The most commonly used lithium salts in battery electrolytes have anions with broadly delocalized negative charge. Lithium bis((trifluoromethyl)sulonyl)imide (LiTFSI) has recently been shown to be a promising salt for Li-ion batteries due to its good conductivity in many electrolyte solvents and its excellent electrochemical and chemical stability. Interestingly, the structurally similar salt, lithium trifluoromethanesulfonate (LiTf), while having similar electrochemical and chemical stability, exhibits poor conductivity in common battery solvents (6). The reasons for the conductivity differences between the LiTFSI and LiTf salts are not clearly understood, but they undoubtedly are due to differences in the solvent–salt interactions of the two anions. We postulate that the LiTf is more associative, and as such this leads to a greater fraction of the solvent–salt interactions being CIPs and AGGs over a SSIP, which is the optimal solvate for charge transport.

This work is part of a larger effort focused on understanding the impact of salt structure on solvent–salt interactions. In this portion of the overall effort we have focused on the solvation and phase behavior of LiTf in several solvents: ethylene carbonate (EC), gamma-butyrolactone (GBL), and propylene carbonate (PC).

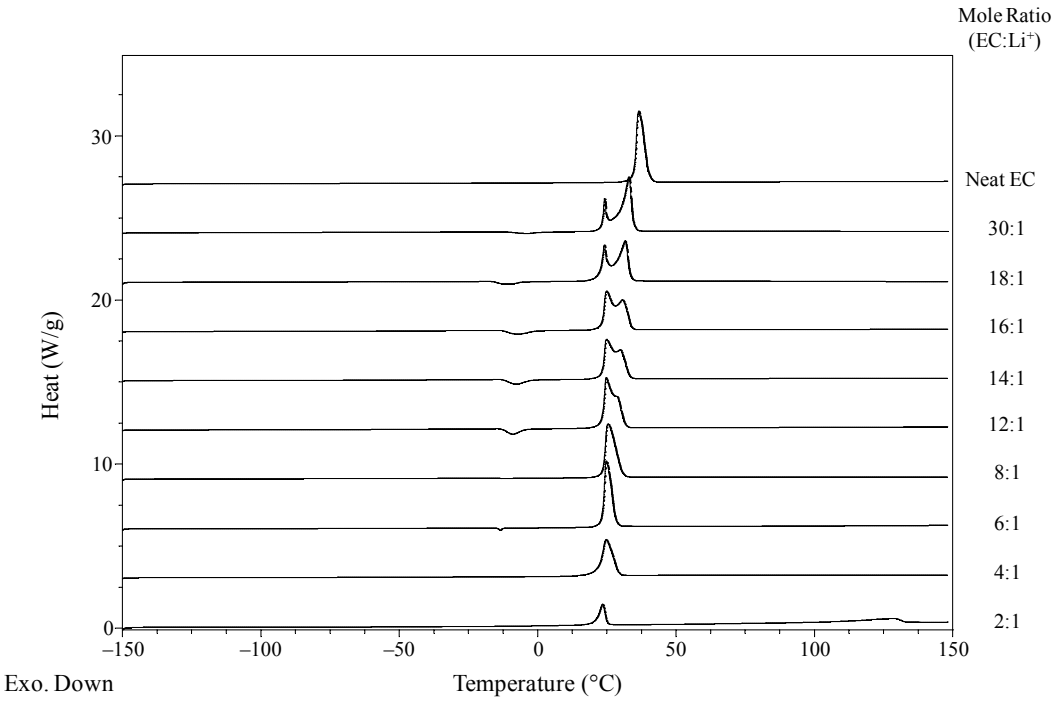

Figure 2. Stack plot of thermograms from analysis of neat EC and EC–LiTf mixtures. Molar compositions are listed along the right-side y-axis (EC:Li^+). Only the final heating trace of 5 °C/min for all data shown.

Our experimental approach involves three analytical technologies. Differential scanning calorimetry (DSC) is applied to gain insight into the phase behavior of solvent–salt mixtures. Raman spectroscopic analysis of solvent–LiTf mixtures enables exploration of solution phase associations and allows us to categorize the solvates into three subgroupngs: SSIP, CIP, and AGG. Finally, the phase behavior information is used to identify molar ratios where it is possible to prepare single phase crystals for interrogation by X-ray diffraction. X-ray data yields unambiguous structural information. In relating all three data sets we gain insight into the solvation and phase behavior of the target solvent–LiTf mixtures.

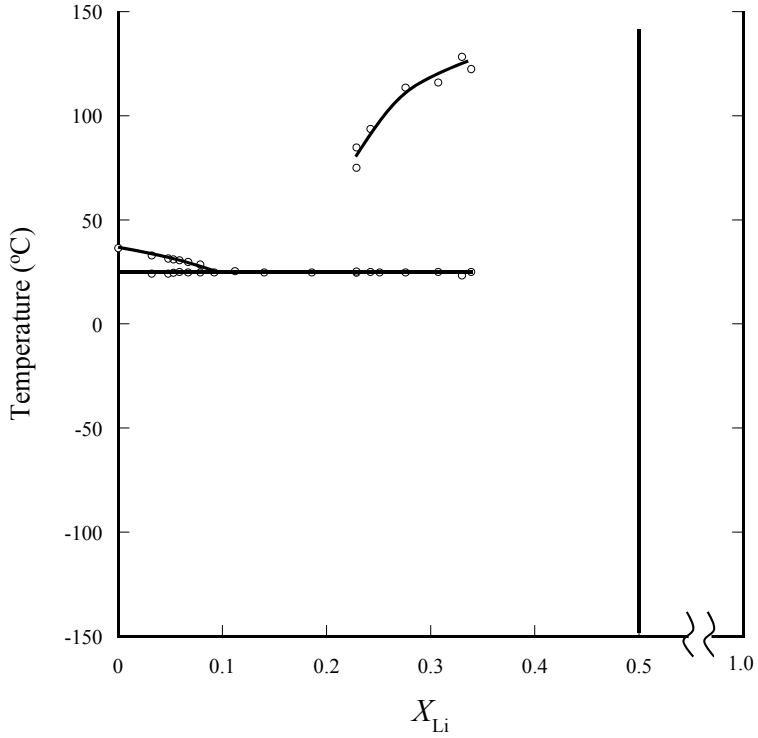

Figure 3. Phase diagram of EC–LiTf. Note the beak in the x-axis between 0.5 and 1.0. The vertical line at 0.5 represents a 1:1 solvate of EC:LiTf.

Results and Discussion

Differential Scanning Calorimetry (DSC)

Mixtures of EC–LiTf were analyzed with the aid of DSC to determine phase behavior. Figure 2 contains a set of thermograms that demonstrate the phase transitions we have so far detected. In the uppermost thermogram, neat EC, one sees the clearly defined melting transition of the pure solvent at 37 °C. Proceeding down the stack plot are mixtures of increasing concentrations of LiTf. Initially, the melting point of EC is depressed to 33 °C and we see the emergence of an additional peak at 24 °C. This lower temperature event is consistent with a phase transition of an EC–LiTf eutectic (8). The phase transition remains nearly constant as the concentration of LiTf increases. In addition to the emergence of the peak at 24 °C, one also notes the decrease in amplitude of the EC melting peak with increase in concentration of LiTf. The shift in peak size is attributed to more EC being associated with the eutectic composition(s) of EC–LiTf. In the thermogram of EC:LiTf at 8:1, the EC melting peak is a barely perceptible shoulder on

the phase transition peak associated with the EC–LiTf eutectic. Interestingly, only in the highest concentration is a peak at 123 °C observed. We attribute this peak to the melting of a 1:1 solvate of EC–LiTf as determined by x-ray crystallography (see below).

Thermal events revealed through DSC analysis are plotted in Figure 3 to generate a phase diagram of the EC–LiTf mixtures. All mixtures examined were solid at room temperature. The more dilute mixtures, $X_{Li} < 0.1$, show 2 thermal events: the melting of EC and a phase transition for a eutectic of EC–LiTf. Mixtures between 0.1 and 0.23 X_{Li} show a single phase transition for an EC–LiTf eutectic. Mixtures more concentrated the 0.23 X_{Li} again show multiple thermal events: one for an EC–LiTf eutectic and a second higher temperature event corresponding to a 1:1 solvate.

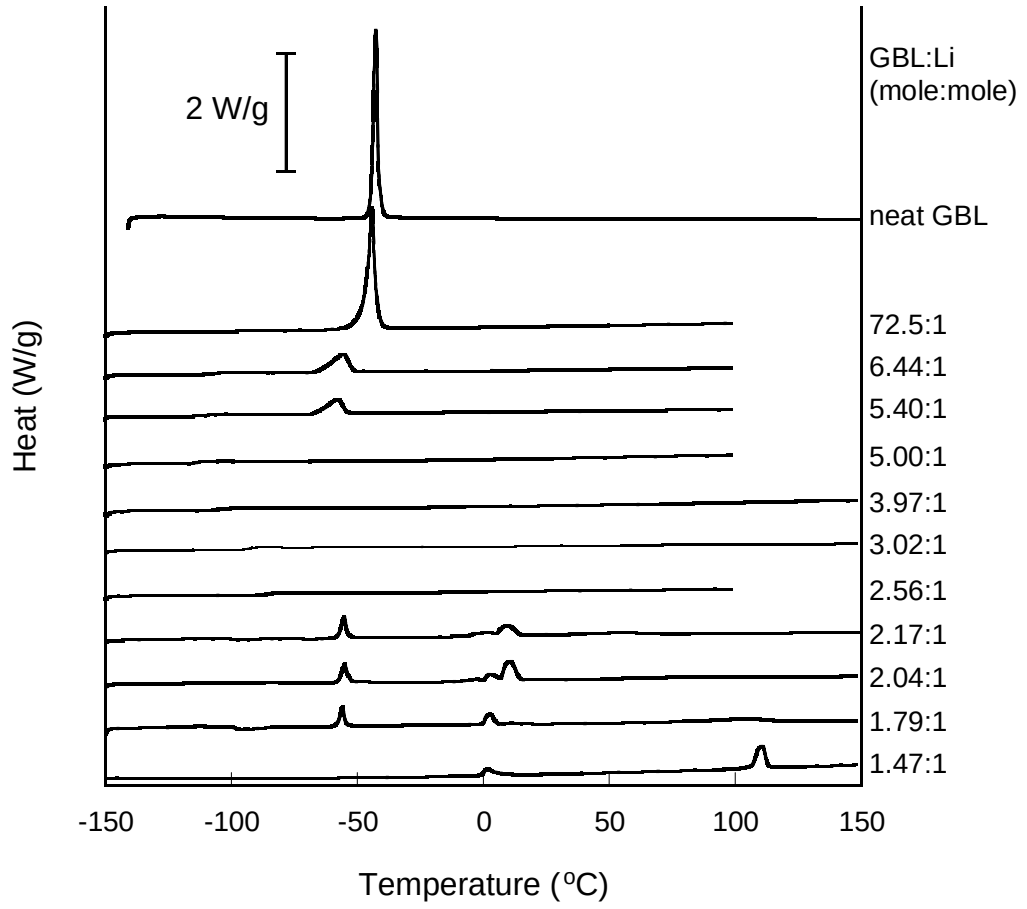

Figure 4. Stack plot of DSC thermograms from analysis of various GBL:LiTf systems. Right y-axis labels indicate the mole ratios of GBL:LiTf going from least to most concentrated, top to bottom. Only final heating curves are shown as samples were annealed with different temperature programs. Data were collected at 5 °C/min from –150 °C to the maximum temperature. Endothermic events are plotted as positive peaks.

Thermograms obtained from DSC analysis of systems of GBL–LiTf are shown in Figure 4 as a stack plot. Inset in the upper left corner of Figure 1 is a y-axis scale bar. Right y-axis values correspond to the composition of the sample analyzed to generate the thermogram aligned with the label. Three distinct concentration regimes give rise to differing system response under thermal perturbation.

In the upper-most thermograms, where lithium cation concentrations are lowest, the melting transition of GBL shifts to more negative temperatures due to freezing point depression. In the thermogram of neat GBL, is a single well defined peak at –42.7 °C that corresponds to the solid–liquid phase transition of the pure solvent. As LiTf salt is added to the GBL solvent, the melting peak shifts to more negative temperatures and becomes broader.

The middle four thermograms, concentrations between 5.00:1 and 2.56:1 GBL:LiTf (mole:mole), do not display any melting transitions. Instead, a concentration dependent glass transition (T_g) is detected. This range of concentrations wherein only a T_g is detected is known as a crystallinity gap (18). Starting from the most dilute sample of 5.00:1 GBL:LiTf (mole:mole), the T_g increases linearly from –116 to –87.5 °C with respect to mole fraction of LiTf in the sample.

Thermograms obtained from measurement of systems with concentrations greater than 2.56:1 GBL:LiTf (mole:mole) show multiple peaks arising from interesting solvent–salt interactions. The thermogram obtained from analysis of the most concentrated system (1.47:1) shows a well defined endothermic peak at 111 °C. We have identified this peak as arising from the melting of a 1:1 solvate. A crystal of the 1:1 solvate was successfully grown and measured with the aid of X-ray diffraction. The crystal structure of the solvate reveals that 6 LiTf ion pair are coordinated to 6 GBL solvent molecules. Li cations are found in a tetrahedral coordination environment consisting oxygen atom lone pair electrons, one from the carbonyl oxygen of the GBL and three from separate Tf anions. This is also sometimes referred to as an aggregate II (AGG_{II}) structure as the Tf anions act as bridging ligands between three separate Li cations (9).

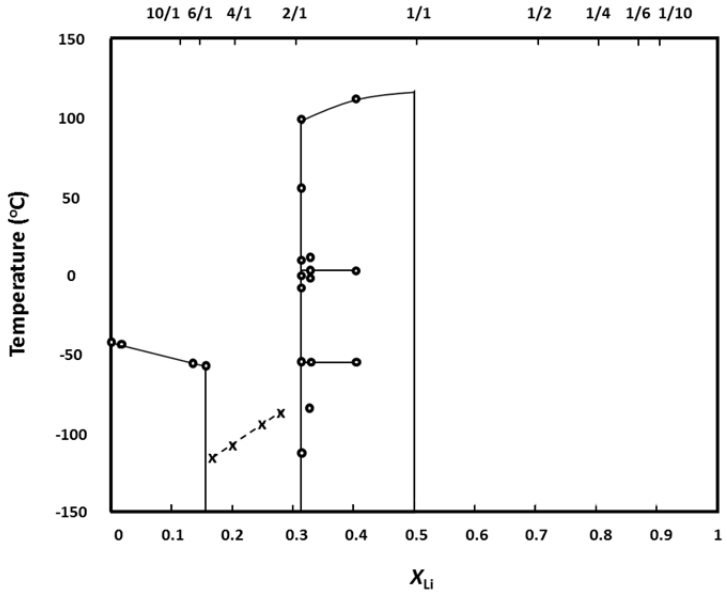

Figure 5. Phase diagram for GBL:$LiCF_3SO_3$ systems. Open circles represent peaks in a thermogram, X marks the T_g, and line indicate melting.

The phase diagram for the GBL:$LiCF_3SO_3$ systems is shown in Figure 5. Melting transitions are shown as lines. At low salt concentrations there is a linear relationship

between the melting point of a mixture and mole fraction of the lithium salt. In the middle region of the diagram is the crystallinity gap where no peaks are detected in the DSC analysis. Sample having a greater mole fraction of lithium salt than those in the crystallinity gap show the typical curved liquidous line in addition to more complex behavior as denoted by the many peaks that were detected.

Presented in Figure 6 are thermograms obtained from the DSC analyses of different mixtures of PC–$LiCF_3SO_3$. Neat PC data is plotted in the bottom thermogram. It is interesting that only neat PC gives evidence of a melting event. The DSC thermograms for the various PC–$LiCF_3SO_3$ mixtures exhibit only a single glass transition (T_g) occurring between –125 and –25 °C. T_g increases as the concentration of $LiCF_3SO_3$ increases. Considering that as the system becomes more concentrated one could expect a greater degree of association between solvated ions, it is reasonable that the T_g increases with increasing salt concentration.

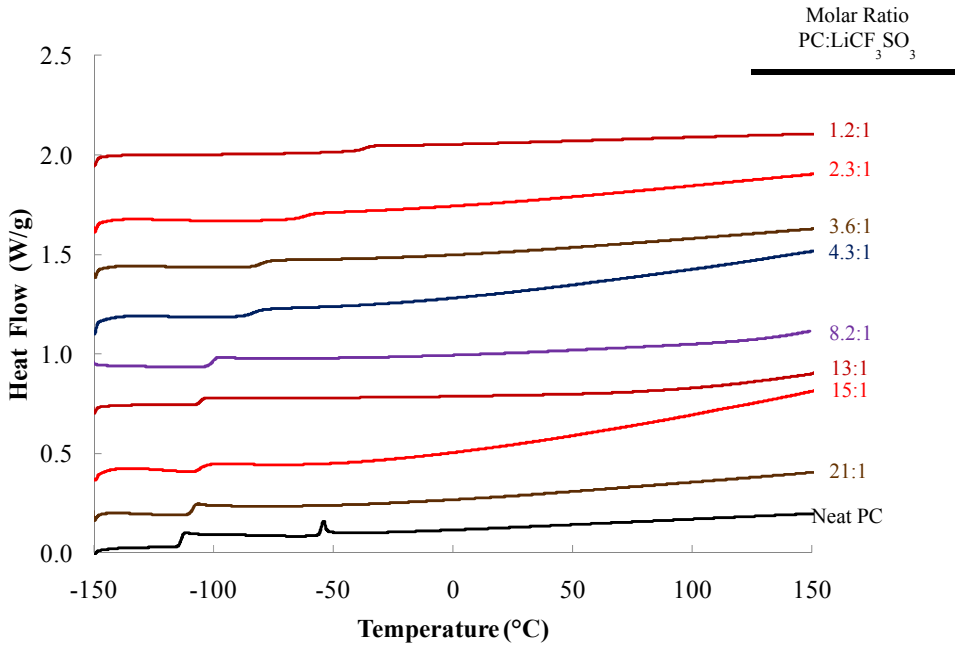

Figure 6. Thermograms from the analysis of different molar ratios of PC–$LiCF_3SO_3$. Exothermic events are positive. Samples were initially equilibrated at –150 °C and then heated at 5 °C/min. On the right y-axis are the concentrations of each mixture.

A phase diagram was constructed from the data obtained by DSC (Figure 7). The only occurrence of a melting event is from analysis of neat PC. For all other mixtures measured, only a single glass transition takes place. The T_g increases linearly with mole fraction of $LiCF_3SO_3$.

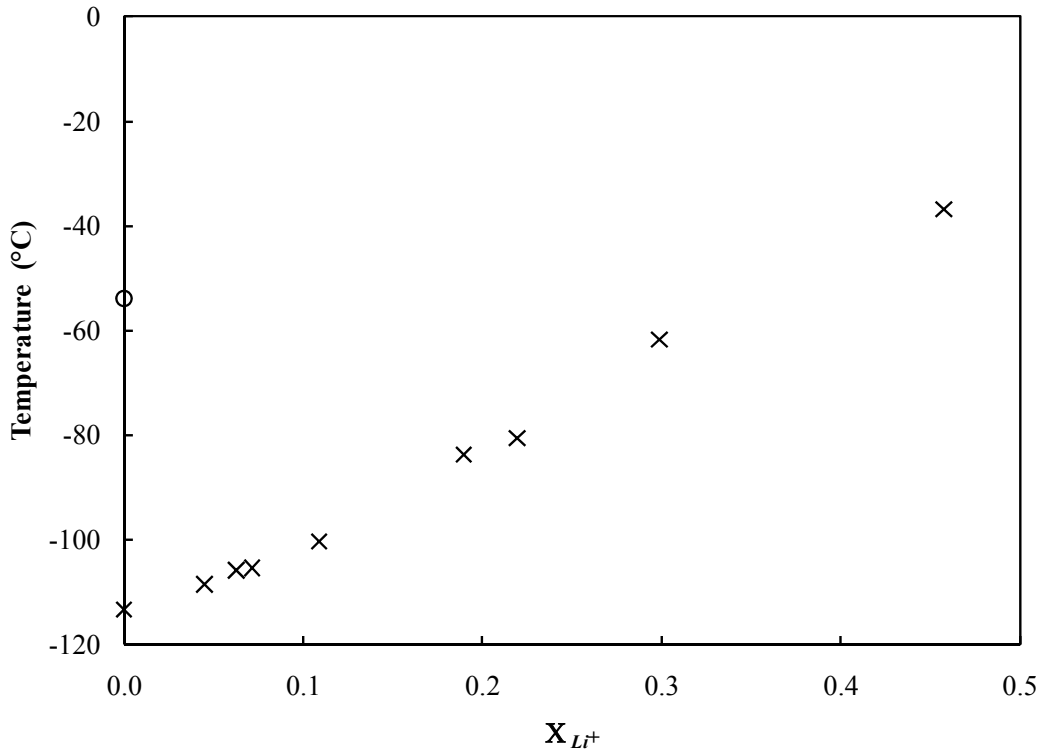

Figure 7. Phase diagram of PC–$LiCF_3SO_3$ derived from thermal analysis of various mixtures. The open circle indicates the melting temperature of neat PC. Large X's mark the T_g's at different mole fractions.

Work with racemic PC, mixtures of PC with LiTf, with the exception of neat PC, DSC results indicated that only glass transitions occur at all molar ratios evaluated. No first-order or solid-solid phase transitions were detected when analyzing mixture containing racemic PC(3). However, when LiTf mixtures with enantiomerically pure PC were analyzed, first-order and solid-solid phase transitions were observed. Additionally, the existence of a 1:1 molar ratio solvate in the most concentrated mixtures was detected (Figures 8 and 9).

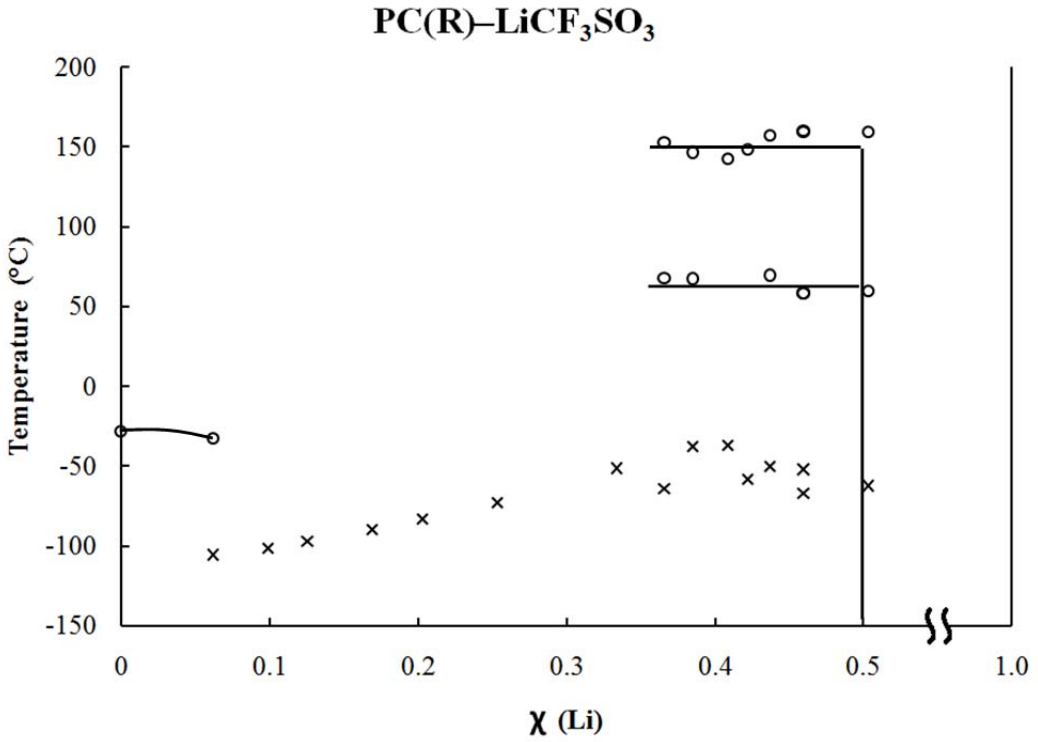

Figure 8. Phase diagram of LiTf in enantiomerically pure PC(R). Open circles represent phase transitions that are either solid-solid or solid-liquid. X's mark temperature, composition data where a glass transition was detected.

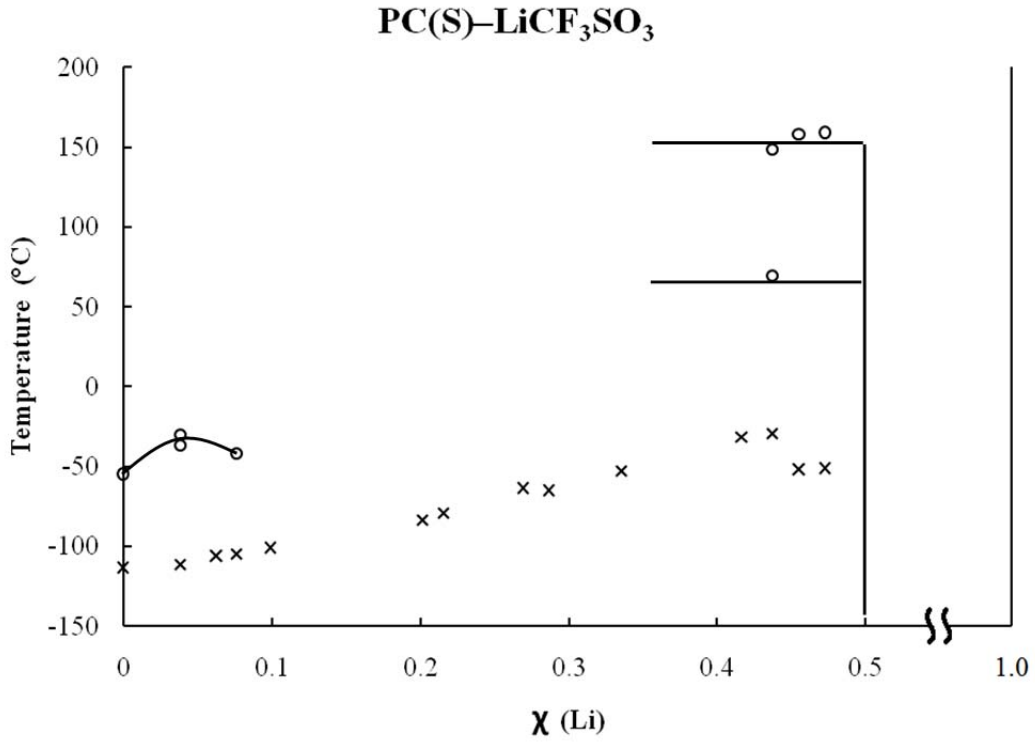

Figure 9. Phase diagram of LiTf in enantiomerically pure PC(S). Open circles represent phase transitions that are either solid–solid or solid–liquid. X's mark temperature,composition data where a glass transition was detected.

Raman Spectroscopy

Probing the mixtures of EC–LiTf with the aid of Raman spectroscopy provides insight into solvation. Figure 10 contains a stack plot of spectra from the Raman spectroscopic analysis of three different molar ratios of EC–LiTf; 1.95:1, 2.26:1 and 3.36:1. Assignments of the symmetric $\delta(CF_3)$ deformation as related to a particular solvate association in glyme–LiTf mixtures were characterized by Frech and coworkers (11). By analogy, the peak at 773 cm^{-1} is attributed to the presence of AGG_{II} association of the Tf^- anion. An AGG_{II} is a solvate where the anion acts as a bridging ligand between three different Li^+ cations. At 764 cm^{-1} is a peak associated with an AGG_I solvate. In an AGG_I solvate the anion, Tf^-, acts as a bidentate bridging ligand between two cations, Li^+. The signature spectral response of a CIP occurs at 760 cm^{-1}. SSIP would appear at ~755 cm^{-1} if present. As there is no peak visible at 755 cm^{-1}, we conclude that LiTf does not form detectable amounts of SSIP when dissolved in EC at the molar ratios investigated in this study to date.

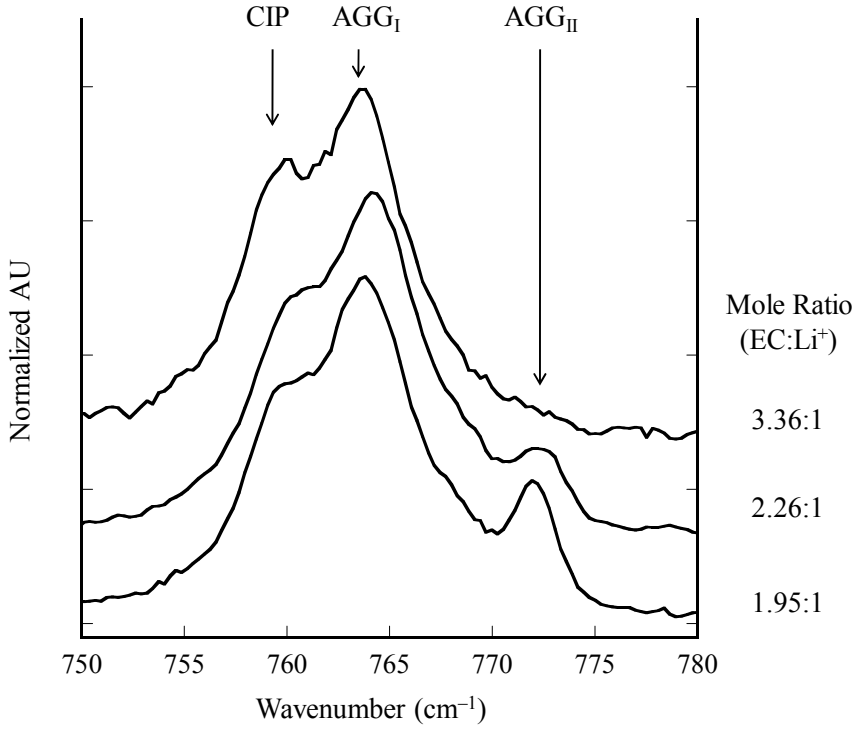

Figure 10. Stack plot of Raman spectra collected at 75 °C for 3 different molar ratios of EC–$LiCF_3SO_3$.

Figure 10 contains data from temperature dependent Raman analysis and a thermogram obtained from measurement of a 2.04:1 GBL:LiTf (mole:mole) sample. The thermogram is plotted with the y-axis temperatures aligned to the temperature of data collection for Raman spectra. Endothermic events are plotted as positive in the x-direction. The sample was initially cooled to –100 °C and equilibrated prior to Raman data collection. After a spectrum was collected the sample was heated in 25 °C increments at 10 °C/min, equilibrated at the new working temperature, and analyzed by Raman spectroscopy.

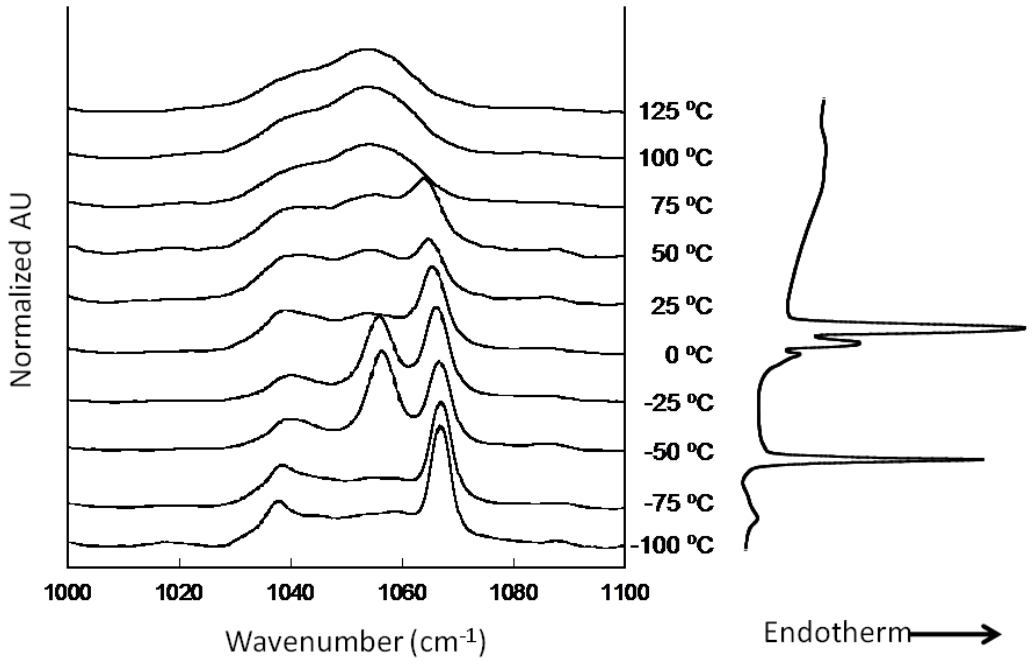

Figure 11. Stack plot of temperature dependent Raman spectra on left with a thermogram plotted to the right. Data were obtained from analyses of a 2.04:1 GBL:LiTf (mole:mole). The right y-axis label corresponds to both the temperature a Raman spectrum was collected at and the temperature axis for the thermogram. Endothermic peaks in the thermogram are plotted as positive in the x-direction.

There is excellent agreement between the thermogram and Raman data in Figure 11. Raman spectra from analysis at –100 and –75 °C are similar. Correspondingly, there is only a small deflection from baseline in the thermogram and therefore no substantial change was expected in solvent–salt coordination. However, upon heating the sample from –75 to –50 °C, there are both dramatic changes in the Raman spectra and a sharp endothermic event in the DSC thermogram. Raman data collect at or below –75 °C show a single peak at 1067 cm^{-1}. The appearance of a well defined peak at 1056 cm^{-1} in the spectrum collected at –50 °C is indicative of a change in coordination of the Tf anion. Upon heating the sample from –50 to –25 °C there is only a slight shift to lower wavenumber for both peaks seen in the –50 °C spectrum which corresponds to a lack of peaks in detected in the DSC analysis. Upon further heating of the sample from –25 to 0 °C, we again find in a dramatic change in Raman signature in agreement with data obtained from calorimetric analysis. The peak a 1056 cm^{-1} is greatly diminished which again indicates a change in coordination of the Tf anion.

Raman spectra from analysis of PC–$LiCF_3SO_3$ mixtures are displayed in Figure 12. The Raman scattering from analysis of neat PC is the uppermost spectrum which has no response. Spectra are stacked with neat PC at the top and increasing concentration of $LiCF_3SO_3$ going down. The bottom spectrum is that of neat $LiCF_3SO_3$.

Working from the bottom to the top, one can see the unperturbed peak for the $\delta(CF_3)$ deformation obtained from analysis of the pure salt. As solvent is added to the sample, the peaks are shifted to smaller wavenumbers. The response associated with AGG_{II} is the greatest at high salt concentration but quickly loses magnitude as solvent molar ratio increases. Clear spectral response arising from the presence of CIP appears at 3.56:1 mole ratio and become the dominant peak as mixtures become more dilute. SSIP remain a minor component even in the most dilute systems.

These data correlate well with the previously discussed DSC data. The smallest addition of salt to the PC solvent results in loss of the endothermic melting event. As the mixtures become more concentrated in salt, the T_g shifts to higher values. This is reasonable in that systems with higher salt concentrations are more aggregated and thus will require more thermal energy to overcome the T_g.

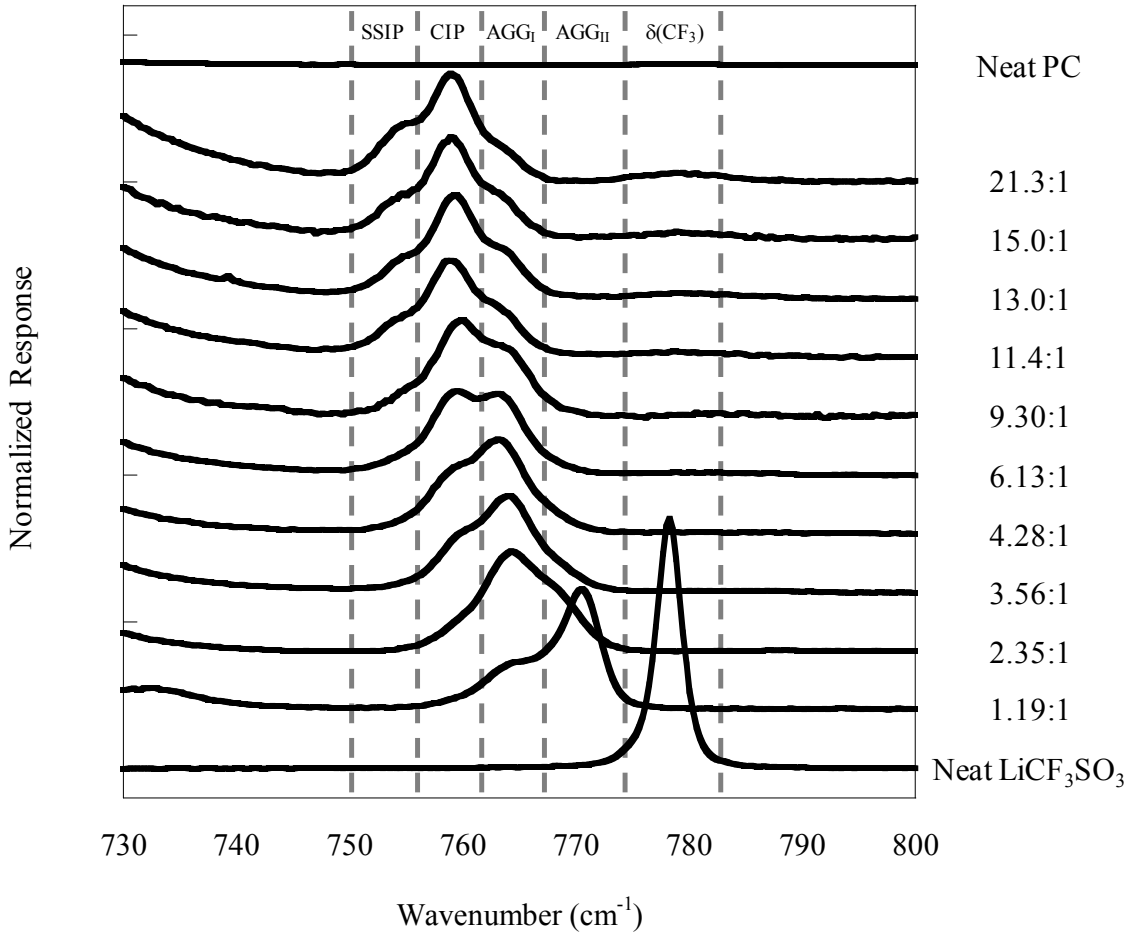

Figure 12. Stack plot of Raman spectra collected at 25 ^oC. Vertical dashed lines indicate the regions where specific $\delta(CF_3)$ deformations occur. Inset along the top x-axis are the solvate categories associated with a spectral region. Along the right y-axis are the molar ratios of the mixtures (PC:$LiCF_3SO_3$).

We also investigated the change in solvate population with respect to change in temperature. Figure 13 is an example of one data set where the molar ratio is fixed and temperature is varied. Three solvates are detected; SSIP, CIP, and AGG_I. The relative

amounts of each solvate category changes with temperature. Assuming that each solvate has an equitable Raman scattering response function, we deconvolute the contribution from each type of solvate and generate a plot which displays how the relative population of a solvate changes with temperature, Figure 14.

Our data indicate that mixtures of PC–$LiCF_3SO_3$ do not crystallize. Additionally, even the most dilute mixtures do not have an appreciable population of SSIP but rather tend towards CIP. Previous work with mixtures of $LiCF_3SO_3$ prepared in the structurally similar solvents γ-butyrolactone or ethylene carbonate yielded very different results. In these solvent–salt mixtures we detected first order phase transitions. Additionally, we were able to isolate single crystals of AGG_{II} category solvates which were subsequently characterized with the aid of x-ray diffraction.

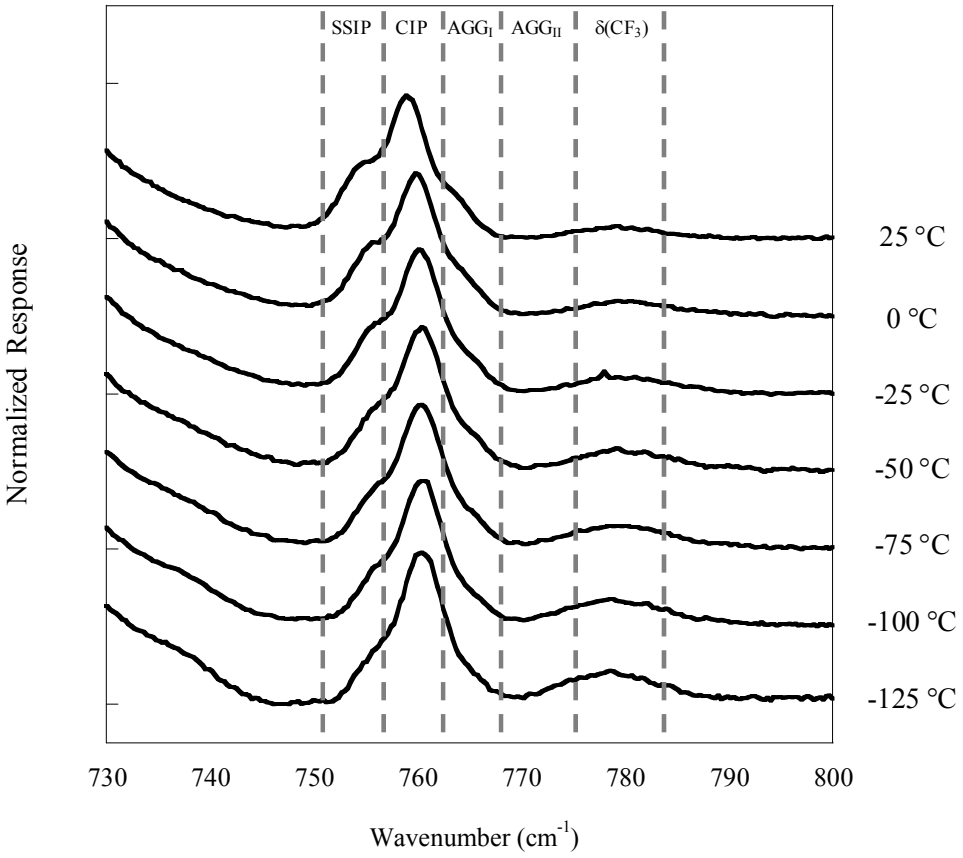

Figure 13. Stack plot of temperature dependent shifts in Raman spectra for a PC–$LiCF_3SO_3$ 21.3:1 mole ratio sample. The temperature at which each spectrum was recorded is listed along the right y-axis.

In trying to understand the behavior being demonstrated by the ions in PC, we have to start with the fact that PC is chiral. The PC used in this study was a racemic mixture of both *R* and *S* enantiomers. The vastly different behavior noted in mixtures where PC is the solvent is due to the presence of both isomers of PC. Polarimetric analysis of the solvent yielded no net optical rotation indicating that the PC was indeed a binary solvent comprised of equal amounts of both isomers, as expected. The additional disorder in PC–$LiCF_3SO_3$ mixtures arising from the structural difference between the *R* and *S* isomers

provides a possible explanation for why PC behaves differently than GBL–$LiCF_3SO_3$ and EC–$LiCF_3SO_3$ mixtures.

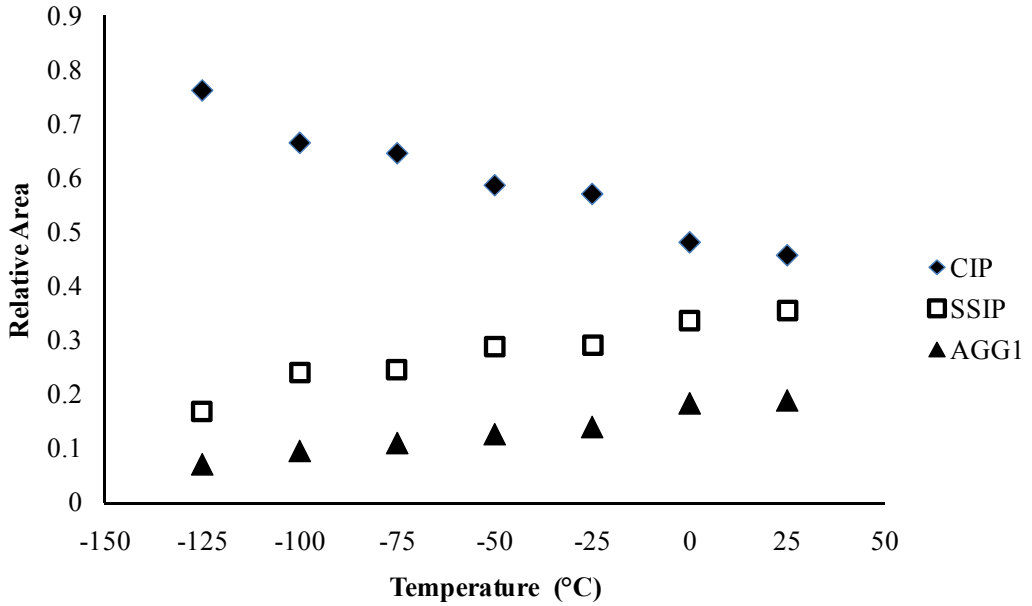

Figure 14. Relative populations of different solvates detected in a 21.3:1 mole ratio mixture of PC–$LiCF_3SO_3$ plotted as a function of temperature.

Analysis of PC–LiTf mixtures revealed the presence of all four categories of solvation. It was also shown that the relative amounts of each type of solvate detected would differ depending upon the temperature and concentration of the mixture. Figure 15 displays a typical Raman spectrum with the full range of data collected. Figure 16 is extracted data from Figure 3 where only the region of the $\delta(CF_3)$ deformation is detected.

Extracted data were processed by the instrument software to fit the signal to the solvation categories: SSIP, CIP, AGG_{II}, and AGG_I. Data were fit to a mix of Lorentzian-Gaussian curves. In order to fit the data some assumptions were made. One was that the previous work by Frech et al. is applicable to the present study. Another assumption is that the scattering response that arises from each solvate is equal. Applying the assumptions, the data are deconvoluted and plotted to show the relative populations of each kind of solvate. The solvates present within a mixture changes with temperature. Figure 17 displays a set of Raman deconvolution data for a 9.96 molar ratio system.

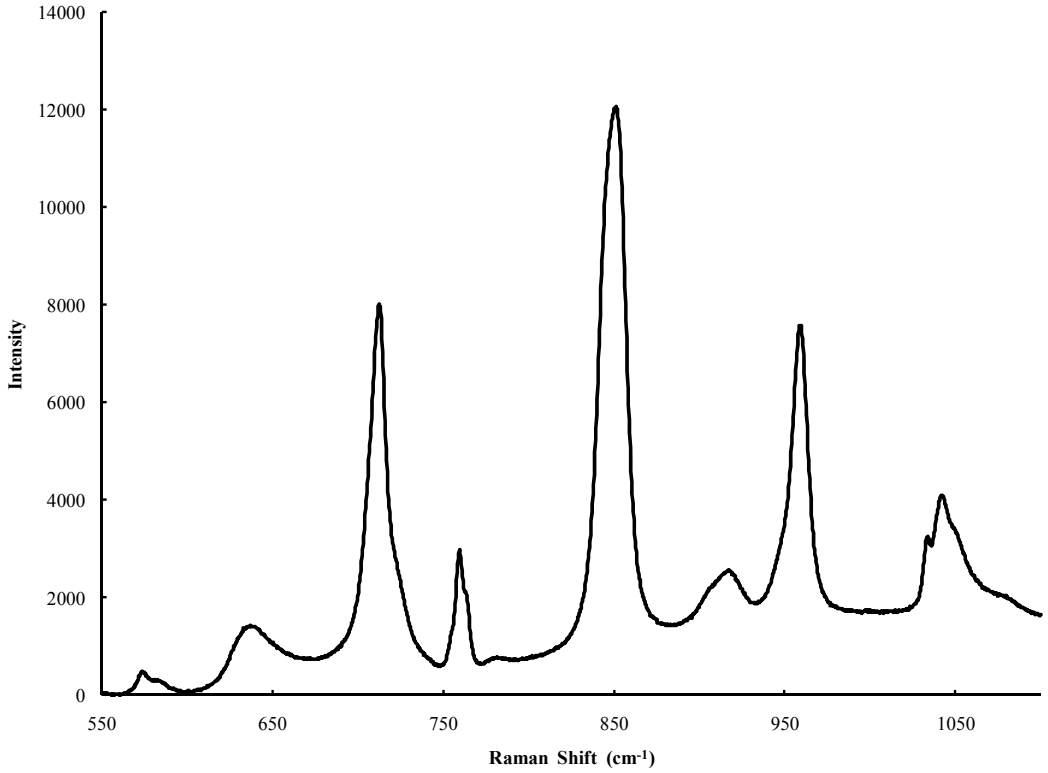

Figure 15. Raman spectrum of a 9.96 mole ratio PC(R):Li (χ_{Li} = 0.091) collected at 0 °C.

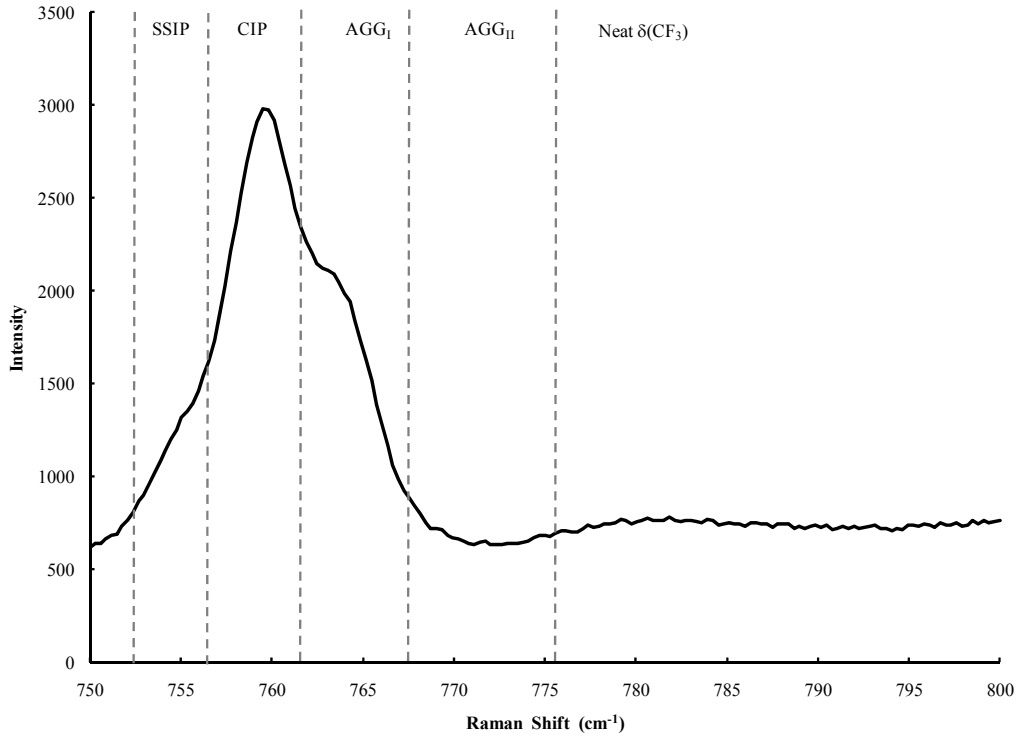

Figure 16. Raman spectrum of a 9.96 mole ratio PC(R):Li (χ_{Li} = 0.091) collected at 0 °C expanded to display the region of the $\delta(CF_3)$ deformation. Dashed lines indicate regions which correspond to the Raman scattering response of the four types of solvates. Annotations across the top of the spectrum indicate where the solvate response occurs.

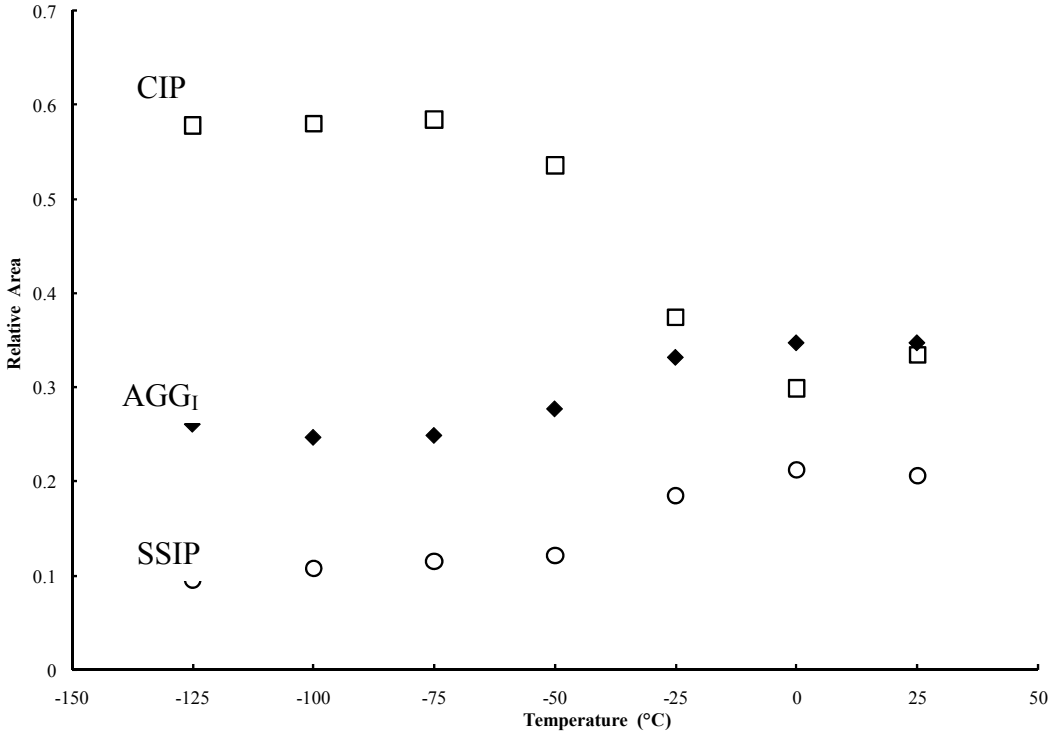

Figure 17. Deconvolution data for a mixture of PC(R)-LiTf at 9.96 molar ratio (χ_{Li} = 0.091). The symbols in the plot: ○, □, and ♦ mark the relative populations of SSIP, CIP, and AGG_I, respectively.

Presenting the data as in Figure 17 reveals something about the nature of the model electrolyte PC(R)–LiTf. The CIP represents the main solvation state at low temperatures. At temperatures above –50 °C, CIP begins to decrease as SSIP and AGG_I increase. It is likely that the entropy of the system is driving these changes in solvation but further work is needed.

X-ray Diffraction

Phase behavior of LiTf mixtures in EC, GBL, and PC(R) indicated the presence of a solvate with a melting temperature between ~120 and 150 °C. Single crystals of each of these high melting solvates were isolated from a mixtures of nearly 1:1 molar ratio of solvent to salt. Figures 18, 19, and 20 display the results of the X-ray diffraction analysis. Lithium ions are coordinated to oxygen atoms from both solvent and Tf-anions. The carbonyl-O of EC is the coordination site of the solvent. Anions act as tridentate bridging ligands coordinated to three separate Li-cations. All of the crystals fall into the AGG_{II} crystal structure category.

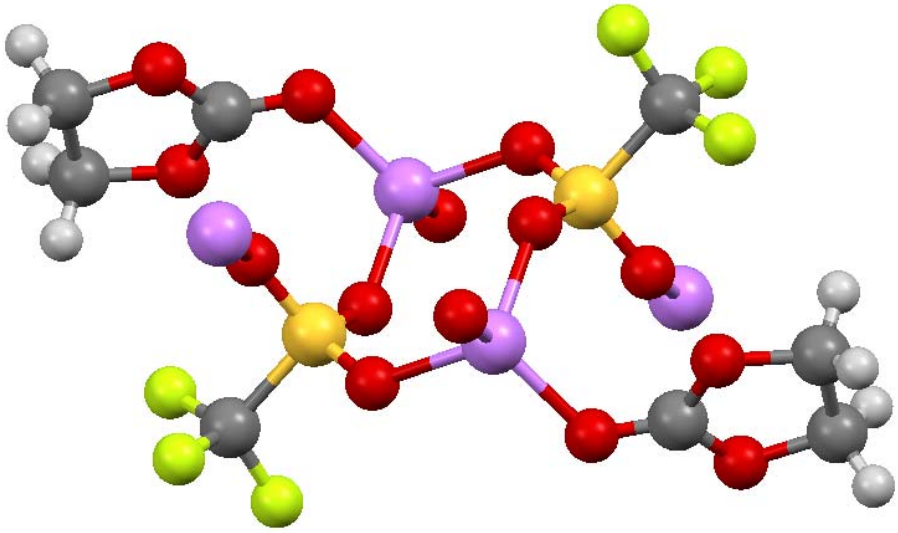

Figure 18. Crystal structure of EC–LiTf, 1:1 molar ratio, AGG_{II} structure category.

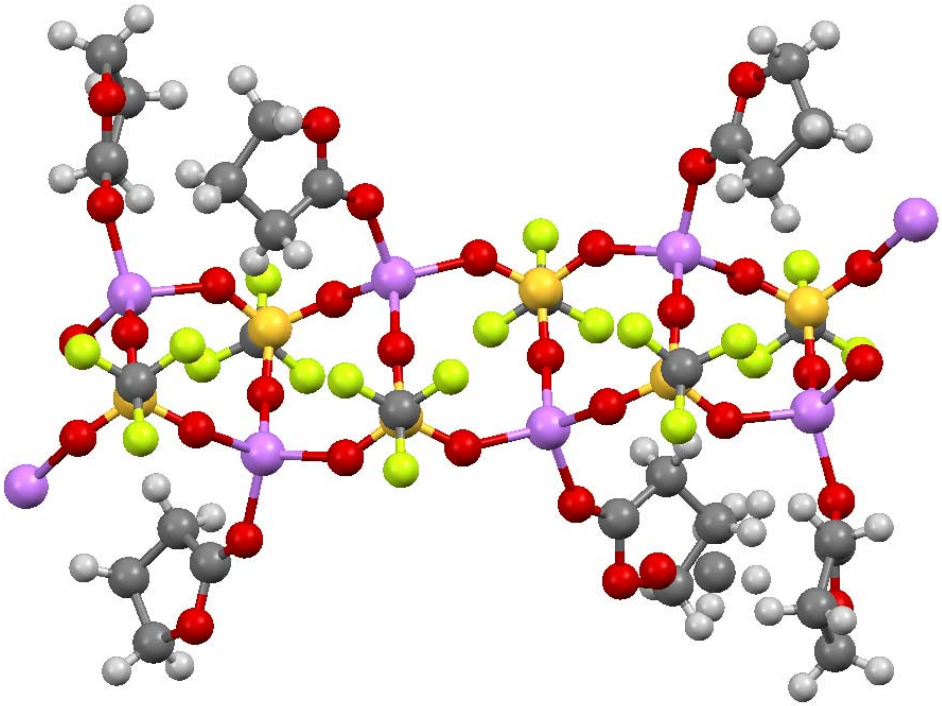

Figure 19. Crystal structure of EC–LiTf, 1:1 molar ratio, AGG_{II} structure category.

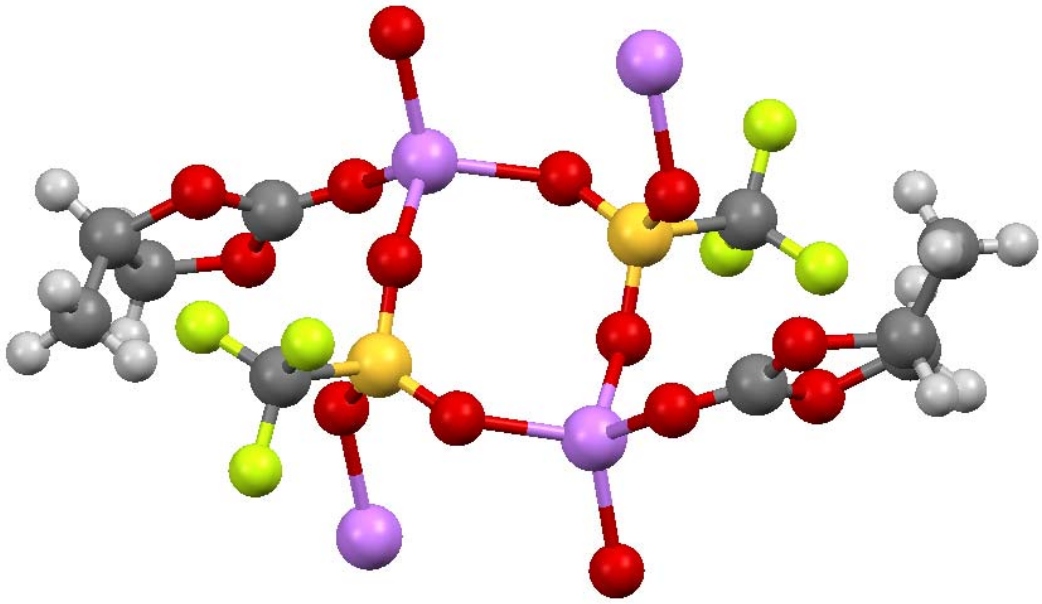

Figure 20. Crystal structure of PC(R)–LiTf, 1:1 molar ratio, AGG_{II} structure category.

Conclusion

Thermal analysis of the various solvent–LiTf mixtures revealed the phase behavior of the model electrolytes was strongly dependent on solvent symmetry. The point groups of the solvents were (in order from high to low symmetry): C_{2V} for EC, C_S for GBL, and C_1 for PC(R). The low symmetry solvents exhibited a crystallinity gap that increased as solvent symmetry decreased; no gap was observed for EC–LiTf, while a crystallinity gap was observed spanning 0.15 to 0.3 mole fraction for GBL–LiTf, and 0.1 to 0.33 mole fraction for PC(R)–LiTF mixtures. Raman analysis demonstrated the dominance of aggregated species in almost all solvent compositions. The AGG and CIP solvates represent the majority of the species in solutions for the more concentrated mixtures, and only in very dilute compositions does the SSIP solvate exist in significant amounts. Thus, the poor charge transport characteristics of CIP and AGG account for the low conductivity and transport properties of LiTf and explain why is a poor choice as a source of Li^+ ions in a Li-ion battery.

5. Papers in which DOE support is acknowledged:

- Matthew P. Foley, Christopher J. Worosz, Kurt D. Sweelya, Luke M. Haverhals. Wesley A. Henderson, Hugh C. De Long, and Paul C. Trulove, "Structure, Disorder, and Crystallization: Lessons Learned from Analysis of Lithium Trifluoromethanesulfonate," ECS Transactions, submitted

- Matthew P. Foley, Daniel M. Seo, Christopher J. Worosz, Paul D. Boyle, Wesley A. Henderson, Hugh C. De Long, and Paul C. Trulove, "Phase Behavior and Solvation of Lithium Triflate in Ethylene Carbonate," ECS Transactions, 41 (27), 99 – 105 (2012).
- Matthew P. Foley, Daniel M. Seo, Paul D. Boyle, Wesley A. Henderson, H. C. De Long, and Paul C. Trulove, "Phase Behavior and Solvation of Lithium Triflate γ-Butyrlactone," *ECS Transactions*, **35** (29), 3 – 8 (2011).

6. People working on the project:

- Dr. Paul C. Trulove (PI) – (1 month/yr, 8.33%)
- Dr. Matthew P. Foley (Assistant Research Professor – Full Support)
- MIDN 1/C Christopher Worosz (undergraduate student) – (0 %).

References

1. B. Y. Liaw and R. Kostecki, *The Electrochemical Society's Interface*, **20**(3), p. 41 (2011).
2. C. J. Allen, Q. Jia, C. N. Chinnasamy, S. Mukerjee, and K. M. Abraham, *J. Electrochem. Soc.*, **158**(12), p. A1250 (2011).
3. G. G. Min, Y. Ko, Tae-Hee Kim, Hyun-Kon Song, S. B. Kim, and Su-Moon Park, *J. Electrochem. Soc.*, **158**(12), p. A1267 (2011).
4. Y. S. Jung, A. S. Cavanagh, Y. Yan, S. M. George, and A. Manthiram, *J. Electrochem. Soc.*, **158**(12), p. A1298 (2011).
5. A SciFinder® search on the term "electrolyte solvation" returns only 67 references. Only 11of the 67 references are related to lithium.
6. K. Xu, *Chem. Rev.*, **104**(10), p. 4303 (2004).
7. H. A. Berman, H. J. C. Yeh, and T. R. Stengle, *J. Phys. Chem.*, **79**(23), 2551 (1975).
8. M. P. Foley, D. M. Seo, P. D. Boyle, W. A. Henderson, H. C. De Long and P. C. Trulove, *ECS Trans.*, **35**(29), 3 (2011).
9. D. M. Seo, P. D. Boyle, and W. A. Henderson, *Acta Cryst.*, E**67**, m1148 (2011).
10. D. M. Seo, T. Afroz, Q. Ly, M. O'Connell, P. D. Boyle, and W. A. Henderson, *ECS Trans.*, submitted.
11. W. Weiwei, R. Frech, and R. A. Wheeler, *J. Phys. Chem.*, **98**, p. 100 (1994).
12. J. Barthel and H. J. Gores in *Handbook of Battery Materials*, J. O. Besenhard, Editor, Wiley-VCH, NY (1999)
13. S. Schantz, M. Kakihana, L. M. Torell and J. R. Stevens, *J. Chem. Phys.*, **92**, 6271 (1990).
14. S. Schantz, M. Kakihana, L. M. Torell and J. R. Stevens, *J. Chem. Phys.*, **94**, 6296 (1991).
15. S. Schantz, M. Kakihana, L. M. Torell and J. R. Stevens, *J. Chem. Phys.*, **94**, 6862 (1991).
16. J. P. Manning and R. Frech, *Polymer*, **33**, 3487 (1992).
17. J. R. Stevens and P. Jacobsson, *Can. J. Chem.*, **69**, 1980 (1991).
18. A. Bernson and J. Lindgren, *Solid State Ionics*, **60**, 31 (1993).

19. W. Huang, R. Frech, P. Johansson and J. Lindgren, *Electrochimica Acta*, **49**, 2147 (1995).
20. W. Huang, R Frech and R. A. Wheeler, *J. Phys. Chem.*, **98**, 100 (1994).
21. J. Hyun, H. Dong, C. P. Rhodes, R. Frech and R. A. Wheeler, *J. Phys. Chem. B*, **105**, 3329 (2001).
22. R. A. Sanders, R. Frech and M. A. Khan, *J. Phys. Chem. B*, **107**, 8310 (2003).
23. R. A. Sanders, R. Frech and M. A. Khan, *J. Phys. Chem. B*, **108**, 2186 (2004).
24. R. A. Sanders, R. Frech and M. A. Khan, *J. Phys. Chem. B*, **108**, 12729 (2004).
25. N. M. Rocher, R. Frech and M. A. Khan, *J. Phys. Chem. B*, **109**, 20697 (2005).
26. C. M. Burba, N. M. Rocher and R. Frech, *J. Phys. Chem. B*, **113**, 11453 (2009).
27. R. Frech and W. Huang, *Macromolecules*, **28**, 1246 (1995).
28. R. Frech, *Macromolecules*, **33**, 9432 (2000).
29. W. A. Henderson, *J. Phys. Chem. B*, **110**, 13177 (2006).